Materials Advances

ROYAL SOCIETY OF CHEMISTRY

PAPER

View Article Online
View Journal | View Issue

Cite this: *Mater. Adv.*, 2025, 6, 5877

Unravelling the crystallization mechanism and structural evolution of Yb/Er-doped SiO_2-GdF_3 nano-glass ceramics†

C. E. Secu, C. Bartha and M. Secu *

The crystallization mechanism of Yb/Er-doped GdF_3 nanocrystals in silica nano-glass ceramics was analyzed using model-free and model-fitting methods and thermal analysis data in correlation with structural data. The formation of GdF_3 nanocrystals occurs at around 300 °C, and their size is temperature dependent, ranging from 14 to 40 nm, depending on the processing temperature. A similar trend is observed for cell volume, where a contraction of up to ≈2.3% (at 600 °C) was assigned to the gradual incorporation of Li and Yb,Er dopants. Model-free analysis showed an increase in activation energy (E_a) and the preexponential factor ($\log A$) up to 175 kJ mol^{-1} and 14.8 s^{-1}, respectively, until the completion of crystallization. Model-fitting analysis indicated a crystallization process controlled by an autocatalytic-type reaction where a second metastable phase (LiF) acts as a catalyst and facilitates a rapid and self-accelerated crystallization of the main GdF_3 nanocrystalline phase. The ceramization process boosted UC luminescence up to values comparable to those of $NaYF_4$:18Yb/2Er.

Received 18th April 2025,
Accepted 1st July 2025

DOI: 10.1039/d5ma00377f

rsc.li/materials-advances

1. Introduction

A novel class of nanostructured materials is represented by nano-glass-ceramics (or glass ceramics), where partial precipitation of a specific nanocrystalline phase within the amorphous glass is reached; nucleation and growth of nanocrystals occur in the parent glass matrix during subsequent thermal processing of the glass.[1] The sol–gel approach represents an easy and controllable method for the preparation of transparent nano-glass ceramics, where optically active nanocrystals are embedded in a glass matrix, and optical transparency is assured by the small size of the nanocrystals.[2,3]

The optical properties of glass ceramics are widely recognized to be significantly influenced by their microstructure, which is directly related to the crystallization process. While these materials have been widely studied for their properties, only a limited number of studies have investigated their crystallization mechanisms and the relationship between these mechanisms and their optical properties.[4,5] For the design of novel and/or improved application-based glass ceramic phosphors, a comprehensive study on the crystallization mechanism is complex but crucial as it can provide valuable insights into their structure and microstructure, as well as into how their structural and optical properties can be controlled through processing. It has been shown that formation of nano-glass ceramics involves a thermally activated chemical decomposition reaction of metal trifluoroacetates precursors, followed by the precipitation and growth of nanocrystals at high temperatures.[2–5] Therefore, the nanocrystal formation process indicates thermal behaviors that can be analyzed through complex thermal analysis, which should include not only TG-DSC measurements but also thermokinetic analysis. The crystallization mechanism under non-isothermal conditions has been investigated through DTA or DSC analysis, based on models such as Avrami's theory, along with modified formulations of the Ozawa, Friedman, Matusita, or Kissinger equations.[6–8] Non-isothermal crystallization kinetic analysis of the β-PbF_2 or YF_3 crystalline phase in silicate glass ceramics indicated a diffusion-controlled process of three-dimensional growth with decreasing nucleation.[4,5] In contrast, we showed that BaF_2 nanocrystal precipitation in a glass matrix is controlled by a homogeneous crystallization mechanism: nucleation centers resulting from thermal decomposition of Ba–trifluoroacetate grow into BaF_2 nanocrystals at higher temperatures—a process revealing a distinct crystallization peak at high temperatures.[9] Later, the same approach was used for the analysis of the crystallization mechanism of an SiO_2-LaF_3 xerogel, and a chemical decomposition reaction followed by the fast precipitation of crystals was proposed instead of a diffusion-controlled nucleation and growth process.[10]

National Institute of Materials Physics, Bucharest-Magurele, Romania.
E-mail: mihail.secu@infim.ro

† Electronic supplementary information (ESI) available. See DOI: https://doi.org/10.1039/d5ma00377f

The synthesis and optical/luminescence properties of glass ceramics with rare-earth doped GdF_3 nanocrystals have been of keen interest for multicolor emitting phosphor applications[11] owing to several advantages such as efficient energy transfer between Gd and RE-ions,[12,13] and the low phonons energy of GdF_3 (around 300 cm^{-1})[14] that assures reduced multi-phonon relaxation rates, all of which lead to highly efficient luminescence properties. In addition, considering their desirable feature, such as low phonon energy,[14] Yb/Er-doped GdF_3 nanocrystals have been investigated for up-conversion (UC) luminescence properties;[15,16] sequential absorption of two or more low energy photons (in infrared range) leads to light emission in the visible range, *i.e.* UC luminescence. However, the Yb/Er-doped GdF_3 nanocrystals showed a tendency to aggregate and exhibited relatively poor UC properties, with enhancement being observed only after Li doping.[15,16] Hence, in order to obtain higher UC luminescence efficiency, it is necessary to choose a proper synthesis method for nanoparticle dispersion along with low phonon energy host for high RE^{3+} ion luminescence efficiency.

A viable way may be to use a sol–gel chemistry approach useful for a wide range of compositions, assuring uniform distribution of optically active nanocrystals within the sample volume (through a thermally activated reaction) without agglomeration effects and with a high transparency degree due to their small size (tens of nm size).[2,3] Investigations into RE^{3+}-doped SiO_2-GdF_3 glass ceramics have demonstrated the precipitation of GdF_3 nanocrystals in a silica matrix.[11,13,17] The crystallization process of GdF_3 nanocrystals (showing hexagonal or orthorhombic structure) is related to the gadolinium trifluoroacetate $Gd(CF_3COO)_3$ decomposition chemical reaction[12] and driven by Li ion dopants.[17] Our investigations highlighted an autocatalytic process where a second metastable phase (lithium fluoride) acts as a catalyst for the GdF_3 crystallization process. Hence, the crystallization mechanism seems to be different compared with metal halide[4,5] nanocrystal precipitation in glass crystallization, but it nevertheless remains incompletely understood.

The aim of this study is to extend our previous knowledge on crystallization processes of GdF_3 nanocrystals in a silica glass matri[17] and the UC luminescence properties using a deep and quantitative approach in order to provide further information that could either complement or confirm it. Model-free and model fitting methods were used to compute the kinetic parameters and propose a reaction model function using differential scanning calorimetry (DSC) data in correlation with data obtained from X-ray diffraction measurements. The absolute quantum yield QY of UC-luminescence of the Yb/Er-doped SiO_2-GdF_3 is also investigated.

2. Materials and methods

2.1. Sample preparation

For the preparation of the undoped and $4Yb^{3+}/1Er^{3+}$-doped $90SiO_2$-$5GdF_3$ (mol%) xerogels and those co-doped with Li, we used the sol–gel synthesis route[17] and reagent-grade tetraethylorthosilicate (TEOS), trifluoroacetic acid (TFA), ethylalcohol, metal acetates, acetic acid and deionized water as starting materials. In the first step, TEOS was hydrolyzed under constant stirring with a mixed solution (8.2 mL) of ethanol and water and using glacial acetic acid as catalyst; molar ratio was 1 : 4 : 3.5 : 0.5. A second solution (3 mL) of $Yb(CH_3COO)_3$, $Er(CH_3COO)_3$, $Li(CH_3COO)$, $Gd(CH_3COO)_3$ and TFA with a Yb : Er : Li : Gd : F molar ratio of 3 : 0.7 : 3.6 : 3.6 : 89 was prepared, mixed and added dropwise to the first solution. After an additional vigorous stirring for 1 h at room temperature, the mixed solution was aged at room temperature for a week in a Petri dish. The wet gels were dried up to 120 °C during 1 week to form the xerogel, and glass ceramization was achieved after thermal calcination in air for 60 min at 525 °C, and the glass ceramic samples were denoted as GCLiYb/Er.

2.2. Characterization methods

The thermal behaviour of the xerogel was investigated using a Netzsch STA 449 F3 Jupiter simultaneous thermal analyser in the TG-DSC mode. Approximately 25 mg sample was measured in synthetic air (80% N_2, 20% O_2) at heating rates of 5, 10, 15, 20, and 25 °C min^{-1} from room temperature to 900 °C. Experiments were conducted in open alumina crucibles at a gas flow rate of 20 mL min^{-1}. Heat flux sensitivity was ±0.001 mW, and temperature accuracy was ±0.01 °C. Non-isothermal kinetic analysis of the DSC data was performed using Netzsch Thermokinetics 3.1 software (version 072010).

The structural characterization of the materials was performed using X-ray diffractometry (XRD) and a BRUKER D8 ADVANCE type X-ray diffractometer, in focusing geometry, equipped with a copper target X-ray tube and LynxEye one-dimensional detector, in the 15°–65° range with a 0.05° step and 2 s integration time. For the analysis of the XRD patterns, we used PowerCell dedicated software.[18]

Photoluminescence and reflectance spectra were recorded at room temperature using a FluoroMax 4P spectrophotometer and its accessories. Up-conversion (UC) luminescence spectra were recorded under laser light pumping at 980 nm from a laser module (200 mW). For the quantitative measurements of UC luminescence efficiency, we used a 50 mm diameter Thorlabs integrating sphere coupled to a commercial spectrophotometer (Ocean Optics usb2000) (see ESI†).

3. Theoretical background

The kinetics of xerogel crystallization were evaluated using model-free and model-fitting approaches. The model-free method allows the determination of activation energy and the preexponential factor without assuming a specific kinetic model for the crystallization process. In this study, the Friedman model was used. This model plots the natural logarithm of the conversion rate ($\ln(d\alpha/dt)$) against $1/T$ for measurements at different heating rates (β).[19] According to theoretical studies,[20] the equation that describes the relationship between the

reaction rate, reacted fraction, and temperature, independent of the thermal sequence used for experiments, has the following form:

$$\frac{dx}{dt} = A\exp\left(\frac{-E_a}{RT}\right)f(x) \quad (1)$$

where α represents the reacted fraction, A is the Arrhenius pre-exponential factor, R is the gas constant, E_a is the activation energy, $f(x)$ is the kinetic model (which is constant in the model-free analysis), and T is the temperature of the process. In logarithmic form, eqn (1) can be written as follows:

$$\ln\left(\frac{dx}{dt}\right) = \ln(Af(x)) - \frac{E_a}{RT} \quad (2)$$

At a constant value of x, eqn (2) can be written as follows:

$$\ln\left(\frac{d\alpha}{dt}\right) = \text{Const} - \frac{E_a}{RT} \quad (3)$$

According to eqn (3), activation energy (E_a) can be determined from the slope of the plot of $\ln\left(\frac{dx}{dt}\right)$ *versus* the inverse of temperature. The model fitting approach facilitates the identification of the crystallization reaction mechanism by minimizing the differences between experimental and calculated values. Using the kinetic parameters derived from the model-free analysis, the reaction model ($f(x)$), can be determined. The experimental data are then fitted to simulated curves, and through a statistical comparison of the fit for various models, the most suitable model along with its corresponding set of parameters is selected.[21]

4. Results and discussion

4.1. Thermal analysis

The TG-DSC curves of the Yb^{3+}/Er^{3+}-doped SiO_2-GdF_3 xerogel co-doped with Li measured in synthetic air with a heating rate of 10 °C min^{-1} are shown in Fig. 1(a). The DSC curve shows four peaks of different intensities, accompanied by a mass loss, as shown in the TG curve. The first endothermic peak, with a maximum at a temperature of 92 °C, is associated with a minor weight loss of approximately 10 wt%, which is attributed to the evaporation of water and residual organic fragments.

The main process revealed by thermal analysis is the thermolysis of metal (M) trifluoroacetate,[22] and the reaction is characterized by a distinct exothermic DSC peak around 300 °C and a weight loss of approximately 38 wt%. A possible mechanism for this reaction involves the breaking of the C–F bond in trifluoroacetate ligands during thermal processing, leading to the formation of new M–F bonds and subsequent growth of MF_3 nanocrystals.[23] The 300 °C peak was assigned to gadolinium trifluoroacetate $Gd(CF_3COO)_3$ thermolysis with subsequent GdF_3 nanocrystalline phase precipitation[11,17] and overlaps with lithium and RE-trifluoroacetate decomposition, which occurs in the same temperature range.[22]

A much weaker exothermic DSC peak at 550 °C is attributed to the crystallization of the $LiGdF_4$ phase, and the small DSC peak at 810 °C is likely associated with glass melting. At higher heating rates, the crystallization maxima shifted to higher temperatures, and their surface areas increased, as shown in Fig. 1(b). This occurs because faster heating leads to the production of a higher number of crystals within the same time.[10]

4.2. Structural and morphological characterization

The XRD pattern analysis allows tracking structural modifications during the annealing of the Yb^{3+}/Er^{3+}-doped SiO_2-GdF_3 xerogel (Fig. 2). The initial dried xerogel annealed up to 250 °C shows a broad background that is characteristic of the amorphous structure of the silica matrix, but as the annealing temperature increases, extra-diffraction peaks assigned to the nanocrystalline GdF_3 fluoride phase precipitation start to develop. The occurrence of GdF_3 nanocrystals dispersed in the amorphous glassy matrix was confirmed using transmission electron microscopy as well.[17] As is known, GdF_3 exhibits two crystalline structures, orthorhombic (space group *Pnma* (no. 62)) and hexagonal (space group $P6_3/mcm$ (no. 193)), which differ significantly in terms of coordination number, lattice volume, and other parameters. The crystallization of the orthorhombic

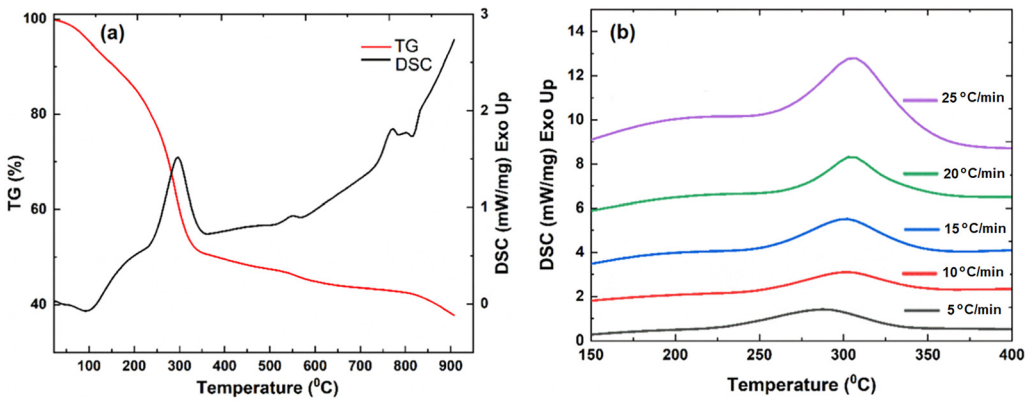

Fig. 1 TG-DSC curves of the Yb^{3+}/Er^{3+}-doped SiO_2-GdF_3 xerogel co-doped with Li, measured in synthetic air at a heating rate of 10 °C min^{-1} (a) and the crystallization peak highlighted at five different heating rates: 5, 10, 15, 20, and 25 °C min^{-1} (b).

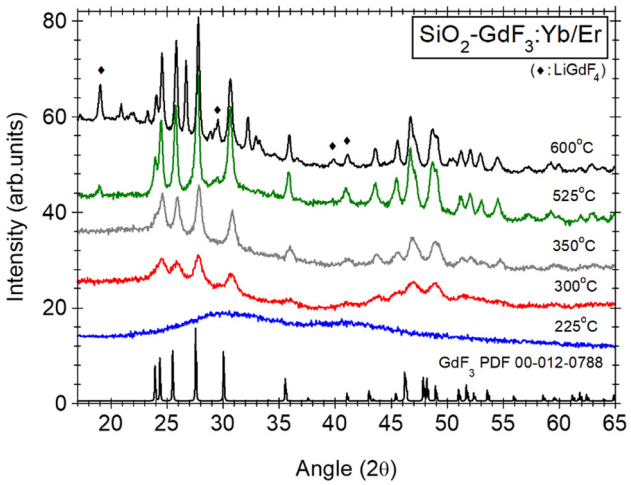

Fig. 2 XRD patterns of GCLiYb/Er glass-ceramic samples after annealing at different temperatures; the XRD pattern of orthorhombic GdF_3 (PDF 012-0788) is included.

GdF_3 nanocrystals (PDF 012-0788) can be observed in the 225–350 °C temperature range and agrees very well with the strong DSC peak at 300 °C from thermal analysis measurements (Fig. 1). At higher temperatures (600 °C), $LiGdF_4$ phase crystallization is observed, accompanied by weaker SiO_2 peaks.

The XRD pattern analysis of the GCLiYb/Er sample annealed at different temperatures according to the TG/DSC curves (Fig. 1) indicates a strong lattice relaxation effect compared with GdF_3 (PDF 012-0788), revealed by the shift to higher angles (Fig. 2), along with a steady increase in the nanocrystals size, up to about 40 nm (Table 1). The ionic radii of 8-fold coordinated Yb^{3+} ions (105.3 pm) and Er^{3+} ions (100.4 pm) are much smaller than that of 8-fold coordinated Gd^{3+} ions (119 pm),[24] and the contraction effect (about 2.3% at 600 °C) was assigned to the Li^+ and Yb^{3+}, Er^{3+} ion incorporation in the lattice. The contraction effect solely related to Yb/Er doping is about 1.4%,[25] and therefore, the additional contraction up to 2.3% is related to Li doping. The contraction effect follows nanocrystal growth, with the unit cell volume decreasing by approximately 1.7% at 300 °C and up to 2.3% at 600 °C, relative to orthorhombic GdF_3 (as shown in Table 1). Hence, we suppose that the contraction effect is due to the incorporation of Li and Yb,Er ions into the lattice during the nanocrystal growth, most likely through the Ostwald ripening mechanism, where the growth of large nanocrystals occurs through the coalescence of smaller ones.

Table 1 Results of the X-ray diffraction (XRD) pattern analysis of GCLiYb/Er glass-ceramic samples annealed at different temperatures; the lattice parameters for GdF_3 (PDF 012-0788) are included for comparison

Temperature (°C)/lattice parameters	a (Å)	b (Å)	c (Å)	Cell volume (Å)^3	D (nm)
275	6.471	6.951	4.430	199.2	14
300	6.471	6.932	4.416	198.1	14
350	6.471	6.933	4.423	198.4	16
525	6.471	6.915	4.407	197.2	25
600	6.471	6.918	4.398	196.9	40
Orth-GdF_3 (PDF file)	6.571	6.984	4.393	201.6	—

4.3. Thermokinetic analysis

4.3.1. Model-free thermokinetic analysis. The activation energy and preexponential factor estimated using Friedman analysis are shown in the Fig. 3.

Model-free analysis indicates that activation energy (E_a) and the preexponential factor ($\log A$) gradually increase up to a partial area (x) of 0.4, reaching values of approximately 171 kJ mol^{-1} and 14.2 s^{-1}, respectively. These parameters remain constant until x reaches 0.8, after which a slow increase is observed. At the end of crystallization ($x = 1$), we obtained an E_a of approximately 175 kJ mol^{-1} and a $\log A$ of about 14.8 s^{-1}. These values are comparable to those reported for YF_3–SiO_2 glass-ceramics, where E_a values of approximately 129 and 139 kJ mol^{-1} were obtained using Kissinger's and Chen's methods, respectively.[5] Similar values of activation energy for PbF_2 crystallization were calculated using the Kissinger method to be about 162 kJ mol^{-1} and 167 kJ mol^{-1} for $x = 0$ and $x = 1$, respectively.[4] In contrast, the E_a value for $80SiO_2$-$90LaF_2$ glass-ceramics is significantly higher, of about 293 kJ mol^{-1}.[10]

4.3.2. Model-fitting analysis. The DSC curves recorded at different heating rates were analyzed and fitted to several reaction models[26] using multivariate least squares regression with the Thermokinetics program. According to Fig. 4, the best-fitted reaction model for the xerogel is the autocatalytic Prout-Tompkins model (Bna).

Previous investigations have shown the Prout-Tompkins autocatalytic model to be useful for describing a crystallization mechanism in which the crystallization rate is influenced by two key factors—the degree of conversion and the presence of catalytic compounds—both of which contribute to accelerating the crystallization process.[26,27] The mathematical representation of this model[28] is given by the following equation:

$$\ln\left(\frac{dx}{dt}\right) = \ln(A) - \frac{E_a}{RT} + n \cdot \ln(1-x) + a \cdot \ln x, \quad \text{with } f(x) = (1-x)^n x^a \tag{4}$$

where n is the order of reaction, and a is the is the autocatalytic constant. The kinetic parameters are listed in Table 2: F_{exp}. is the experimental form of the reaction model ($f(x)$), obtained from DSC data, and the model with an F_{exp}-value of 1 has the least deviation out of all the models compared; F_{crit} is the critical value (quantile), obtained from F-distribution at a significance level of 0.05; t_{crit} is the critical value, obtained from t-distribution, and is defined for a given significance level and degrees of freedom.

According to this model, the amorphous xerogel sample shows rapid self-accelerated crystallization, which occurs through the simultaneous formation of Li-related metastable phases, resulting from the thermal decomposition of metal trifluoroacetates at temperatures around 300 °C. Although these phases are not detected in XRD patterns at this temperature—likely because of their low crystallinity, nanoscale

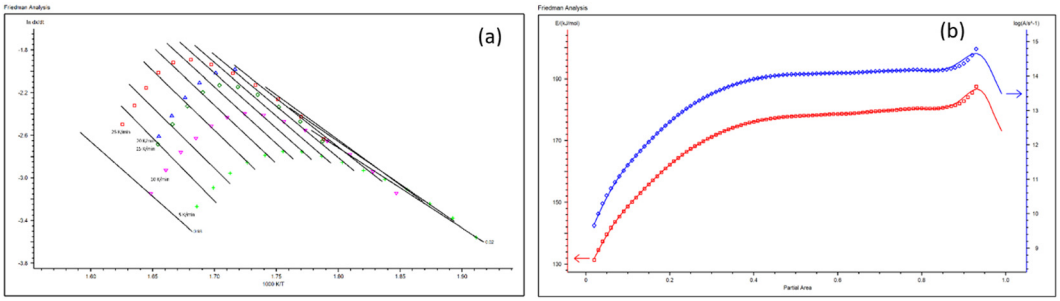

Fig. 3 Friedman analysis of the crystallization of the Yb^{3+}/Er^{3+}-doped SiO_2-GdF_3 xerogel co-doped with Li (a). Dependence of activation energy and the pre-exponential factor on the crystallization fraction according to the Friedman method (b).

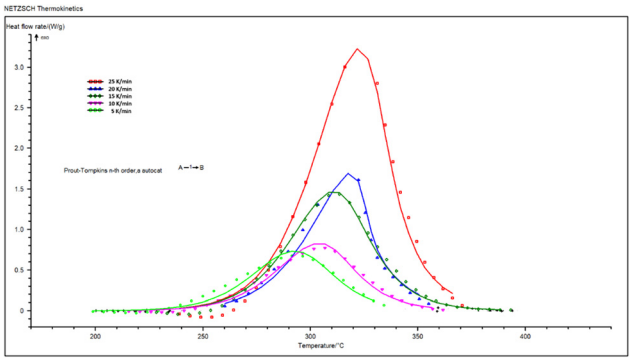

Fig. 4 Experimental data for the Yb^{3+}/Er^{3+}-doped SiO_2-GdF_3 xerogel co-doped with Li and the fitting curve of the 300 °C crystallization peak.

Table 2 Kinetic model parameters resulting from non-linear regression analysis

Parameters	Values
Log A (s^{-1})	12.25 ± 0.67
E_a (kJ mol^{-1})	157.50 ± 2.73
React. Ord. 1	1.574 ± 0.09
Exponent a	0.211 ± 0.006
F_{exp}	1
F_{crit} (0.95)	1.08
Statistical parameters	
Correlation coefficient	0.994
Durbin–Watson factor	2.41
Rel. precision	0.00100
t-Critic (0.95; 136)	1.969

dimensions, or limited concentration[29] —they play a crucial catalytic role in the crystallization process. Li^+ ion doping is favorable for the formation of metastable phases that can act as diffusion barriers or phase interfaces, preventing uncontrolled crystallization kinetics (*e.g.*, by delaying the crystallization of stable phases, blocking volatile pathways that would intensify autocatalysis, modifying diffusion in the solid state, *etc.*). By lowering the activation energy, they facilitate the crystallization of the Yb^{3+}/Er^{3+}-doped SiO_2-GdF_3 phase, thus promoting rapid phase formation. Furthermore, a reaction order value (n) greater than 1 (with $n \approx 1.57$) suggests an accelerated nucleation and crystallite growth rate. This leads to a nonlinear increase in the crystallization rate, which can result in the formation of larger crystallites or rapid development of the crystalline phase. However, if not properly controlled, such conditions may also introduce issues, including structural defects or incomplete crystallization. Statistical parameters indicate that the model fits well, showing a strong correlation, no significant autocorrelation in the residuals, high precision, and statistical significance in the parameter estimates. This is supported by the Durbin–Watson statistic, which tests for autocorrelation in the residuals. A value near 2 indicates no significant autocorrelation.[29] Since the value of 2.41 is close to 2, it suggests that the residuals are independent, which is a positive indication.

4.4. Up-conversion luminescence properties

We observed that Li-ion co-dopant influence is not limited only to crystallization behavior (see above) but also on structural properties (for higher doping levels[25]) accompanied by optical property improvements.[17,25] Under 980 nm IR light pumping, the GCLiYb/Er glass ceramic sample showed UC luminescence of Er^{3+} ions, caused by the energy transfer Yb–Er within the GdF_3 nanocrystals (Fig. 5).

The substitutional Li^+ ions tailor the crystal field symmetry and alter the environment of Er^{3+},[15,16] leading to an increase in

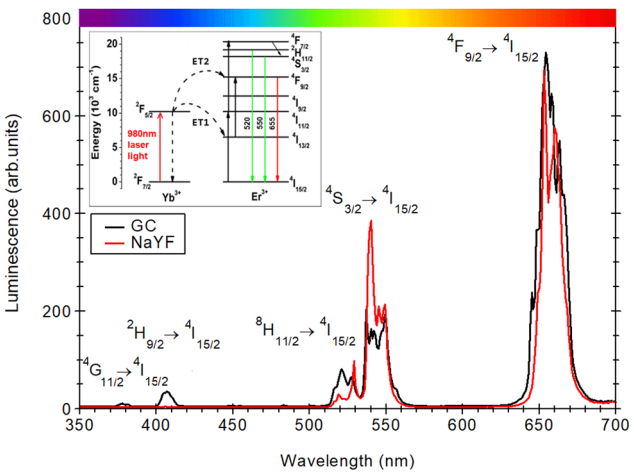

Fig. 5 Normalized UC luminescence spectra recorded for GCLiYb/Er glass-ceramic (after calcination at 525 °C) and β-$NaYF_4$:18Yb/2Er polycrystalline powder recorded under 980 laser light pumping and the possible mechanism with the RE energy levels involved (inset).

UC luminescence.[25] The UC mechanism has been extensively investigated in various host Yb^{3+}/Er^{3+}-doped nanocrystalline host materials, including GdF_3,[15,16] and oxyfluoride glass ceramics.[30–33] It is based on highly efficient IR light absorption by Yb^{3+} ions at around 1000 nm ($^2F_{7/2} \rightarrow {}^2F_{5/2}$ transition). For unsaturated up-conversion processes, the UC luminescence intensity is proportional to the *n*th power of the incident pump power. The value of *n*, corresponding to the number of pump photons required for the population of the emitting level,[34] can be extracted from a double logarithmic plot, luminescence intensity *vs.* incident pump intensity, where *n* is the slope of this dependence (see ESI†). The Er^{3+} emitting levels are feed by the two-photon energy transfer (ET) process, accompanied by multi-phonon and cross-relaxation (Yb^{3+}–Er^{3+}) processes, followed by the characteristic green (($^2H_{11/2}$, $^4S_{3/2}$) $\rightarrow$ $^4I_{15/2}$) and red ($^4F_{9/2} \rightarrow {}^4I_{15/2}$) luminescence (Fig. 5 inset); for ''uv-blue'' up-conversion luminescence ($^4G_{11/2}$, $^2H_{9/2} \rightarrow {}^4I_{15/2}$), three-photon energy transfer processes are involved.[30,33]

The quantitative measurement of the absolute quantum yield (QY) of up-conversion is challenging; therefore, we used the method proposed by J. C. Boyer *et al.*[35] For comparison and verification, we measured β-$NaYF_4$:18Yb/2Er polycrystalline powder, known to show the best luminescence property among UC luminescent materials. We obtained a QY of 0.2 ± 0.1% for GCLiYb/Er glass ceramic, and 0.3 ± 0.1% for the β-$NaYF_4$:18Yb/2Er, which matches well with the values reported in the literature;[35] QY can increase under higher power density.[36] For applications, optical transparency is a very important parameter. In the present case, GCLiYb/Er glass ceramic shows good optical transparency in the blue to red spectral optical range (300–700 nm), as shown by the high reflectance values of about 0.75; the small dips at 377, 485, 519 and 650 nm are assigned to the Er^{3+} ions characteristic absorptions from the ground state $^4I_{15/2}$ to $^4G_{11/2,9/2}$, $^4F_{7/2}$, $^2H_{11/2}$ and $^4F_{9/2}$, respectively (see ESI†).

5. Conclusion

Complex thermal analysis, correlated with structural data, showed that the precipitation of GdF_3 nanocrystals results from the thermolysis of gadolinium-trifluoroacetate at approximately 300 °C. The crystallization mechanism was found to be autocatalytic, with Li-based metastable phases acting as catalysts by lowering activation energy barriers for nanocrystal nucleation and growth. Thermokinetic analysis also indicated an accelerated rate of crystal nucleation and growth, influencing the material structure and microstructure. This behavior was confirmed by the evolution of optical properties, which showed enhanced UC luminescence, reaching values comparable to those of the NaYF4:18Yb/2Er phosphor while maintaining the optical transparency of the material.

Conflicts of interest

There are no conflicts to declare.

Data availability

The experimental data that support the findings of this study will be available on request.

Acknowledgements

The authors acknowledge funding by the Core Program of the National Institute of Materials Physics (NIMP), granted by the Romanian Ministry of Research, Innovation and Digitization through the Project PC3-PN23080303. The help of Dr Silviu Polosan for the Up-Conversion luminescence set-up and efficiency measurements is gratefully acknowledged.

References

1 E. D. Zanotto, A bright future for glass-ceramics, *Am. Ceram. Soc. Bull.*, 2010, **89**(8), 19–27.
2 G. Gorni, J. J. Velázquez, J. Mosa, R. Balda, J. Fernández, A. Durán and Y. Castro, Transparent Glass-Ceramics Produced by Sol–Gel: A Suitable Alternative for Photonic, *Materials*, 2018, **11**(212), 1.
3 M. Secu, C. Secu and C. Bartha, Optical Properties of Transparent Rare-Earth Doped Sol-Gel Derived Nano-Glass Ceramics, *Materials*, 2021, **14**(22), 6871.
4 W. Luo, Y. Wang, F. Bao, L. Zhou and X. Wang, Crystallization behavior of PbF_2–SiO_2 based bulk xerogels, *J. Non-Cryst. Solids*, 2004, **347**, 31–38.
5 W. Luo, Y. Wang, Y. Cheng, F. Bao and L. Zhou, Crystallization and structural evolution of YF3 –SiO2 xerogel, *Mater. Sci. Eng. B*, 2006, **127**, 218–223.
6 Z. Hu, Y. Wang, F. Bao and W. Luo, Crystallization behavior and microstructure investigations on LaF3 containing oxyfluoride glass ceramics, *J. Non-Cryst. Solids*, 2005, **351**, 722–728.
7 D. Chen, Y. Wang, Y. Yu and Z. Hu, Crystallization and fluorescence properties of Nd $^{3+}$ - doped transparent oxyfluoride glass ceramics, *Mater. Sci. Eng. B*, 2005, **123**, 1–6.
8 Y. Yu, D. Chen, Y. Cheng, Y. Wang, Z. Hu and F. Bao, Investigation on crystallization and influence of Nd3+ doping of transparent oxyfluoride glass-ceramics, *J. Eur. Ceram. Soc.*, 2006, **26**, 2761–2767.
9 C. E. Secu, C. Bartha, S. Polosan and M. Secu, Thermally activated conversion of a silicate gel to an oxyfluoride glass ceramic: Optical study using Eu^+ probe ion, *J. Lumin.*, 2014, **146**, 539–543.
10 G. Gorni, M. J. Pascual, A. Caballero, J. J. Velázquez, J. Mosa, Y. Castro and A. Durán, Crystallization mechanism in sol-gel oxyfluoride glass-ceramics, *J. Non-Cryst. Solids*, 2018, **501**, 145–152.
11 J. J. Velázquez, J. Mosa, G. Gorni, R. Balda, J. Fernández, L. Pascual, A. Durán and Y. Castro, Transparent SiO_2 GdF_3 sol–gel nano-glass ceramics for optical applications, *J. Sol-Gel Sci. Technol.*, 2019, **89**, 322–332.
12 H. Guan, Y. Sheng, C. Xu, Y. Dai, X. Xie and H. Zou, Energy transfer and tunable multicolor emission and paramagnetic

properties of GdF_3:Dy^{3+},Tb^{3+},Eu^{3+} phosphors, *Phys. Chem. Chem. Phys.*, 2016, **18**, 19807–19819.
13 N. Pawlik, B. Szpikowska-Sroka, E. Pietrasik, T. Goryczka and W. A. Pisarski, Photoluminescence and Energy transfer in transparent glass-ceramics based on GdF_3:RE^{3+} (RE = Tb, Eu) nanocrystals, *J. Rare Earths*, 2019, **37**, 1137–1144.
14 T. Miyakawa and D. L. Dexter, Cooperative and stepwise excitation of luminescence: trivalent rare-earth ions in Yb^{3+} sensitized crystals, *Phys. Rev. B:Condens. Matter Mater. Phys.*, 1970, **1**, 70–80.
15 H. Wang and T. Nann, Monodisperse upconversion GdF3:Yb, Er rhombi by microwave-assisted synthesis, *Nanoscale Res. Lett.*, 2011, **6**(1), 267.
16 W. Yin, L. Zhao, L. Zhou, Z. Gu, X. Liu, G. Tian, S. Jin, L. Yan, W. Ren, G. Xing and Y. Zhao, Enhanced red emission from GdF_3:Tb^{3+},Er^{3+} upconversion nanocrystals by Li^+ doping and their application for bioimaging, *Chemistry*, 2012, **18**(30), 9239–9245.
17 C. E. Secu, C. Bartha, C. Radu and M. Secu, Crystallization processes of rare-earth doped GdF_3 nanocrystals in silicate glass matrix: Dimorphism and photoluminescence properties, *Ceram. Int.*, 2024, **20**, 37518–37524.
18 W. Krause and G. Nolze, PowderCell a program for the representation and manipulation of crystal structures and calculation of the resulting X-ray patterns, *J. Appl. Cryst.*, 1996, **29**, 301–303.
19 J. M. Criado, P. E. Sanchez-Jimenez and L. A. Perez-Maqueda, Critical study of the isoconversional methods of kinetic analysis, *J. Therm. Anal. Calorim.*, 2008, **92**, 199–203.
20 A. Khawam and D. R. Flanagan, Solid-state kinetic models: basics and mathematical fundamentals, *J. Phys. Chem. B*, 2006, **110**, 17315–17328.
21 E. Moukhina, Determination of kinetic mechanisms for reactions measured with thermoanalytical instruments, *J. Therm. Anal. Calorim.*, 2012, **109**, 1203–1214.
22 Y. Yoshimura and K. Ohara, Thermochemical studies on the lanthanoid complexes of trifluoroacetic acid, *J. Alloys Compd.*, 2006, **408–412**, 573–576.
23 A. C. Yanes, J. Del-Castillo, J. Méndez-Ramos, V. D. Rodriguez, M. E. Torres and J. Arbiol, Luminescence and structural characterization of transparent nanostructures Eu^{3+}-doped LaF_3-SiO_2 glass-ceramics prepared by sol-gel method, *Opt. Mater.*, 2007, **29**(8), 999–1003.
24 R. D. Shannon, Revised effective ionic radii and systematic studies of interatomic distances in halides and chalcogenides, *Acta Crystallogr., Sect. A*, 1976, **32**, 751–767.
25 C. Secu, C. Bartha, C. Radu and M. Secu, M. Up-Conversion Luminescence and Magnetic Properties of Multifunctional Er3+/Yb3+-Doped SiO2-GdF3/LiGdF4 Glass Ceramics, *Magnetochemistry*, 2023, **9**, 11.
26 S. Vyazovkin and C. A. Wight, Model-free and model-fitting approaches to kinetic analysis of isothermal and nonisothermal data, *Thermochim. Acta*, 1999, **340–341**, 53–68.
27 J. M. S. P. Shahi, S. K. Srivastava and R. S. Tiwari, A Study of Crystallization Kinetics of an Amorphous Glass-Ceramic System Using the Prout-Tompkins Model, *J. Non-Cryst. Solids*, 2012, **358**(16), 2170–2175.
28 K. Prout and F. W. Tompkins, The theory of the crystallization kinetics of metals and alloys, *Trans. Faraday Soc.*, 1950, **46**, 791–803.
29 J. Durbin and G. S. Watson, Testing for serial correlation in least squares regression. I, *Biometrika*, 1950, **37**(3–4), 409–428.
30 J. J. Velázquez, G. Gorni, R. Balda, J. Fernández, L. Pascual, A. Durán and M. J. Pascual, Non-Linear Optical Properties of Er^{3+}–Yb^{3+}-Doped $NaGdF_4$ Nanostructured Glass Ceramics, *Nanomaterials*, 2020, **10**(7), 1425.
31 M. Secu and C. E. Secu, Up-conversion luminescence of Er^{3+}/Yb^{3+} co-doped $LiYF_4$ nanocrystals in sol-gel derived oxyfluoride glass-ceramics, *J. Non-Cryst. Solids*, 2015, 42678–42682.
32 A. de Pablos-Martín, J. Méndez-Ramos, J. del-Castillo, A. Durán, V. D. Rodríguez and M. J. Pascual, Crystallization and up-conversion luminescence properties of Er^{3+}/Yb^{3+}-doped $NaYF_4$-based nano-glass-ceramics, *J. Eur. Ceram. Soc.*, 2015, **35**(6), 1831–1840.
33 S. Georgescu, A. M. Voiculescu, C. Matei, C. E. Secu, R. F. Negrea and M. Secu, Ultraviolet and visible up-conversion luminescence of Er^{3+}/Yb^{3+} co-doped CaF_2 nanocrystals in sol–gel derived glass-ceramics, *J. Lumin.*, 2013, **143**, 150–156.
34 M. Pollnau, D. R. Gamelin, S. R. Lüthi and H. U. Güdel, Power dependence of upconversion luminescence in lanthanide and transition-metal-ion systems, *Phys. Rev. B: Condens. Matter Mater. Phys.*, 2000, **61**, 3337.
35 J. C. Boyer and F. C. J. M. van Veggel, Absolute quantum yield measurements of colloidal $NaYF_4$: Er^{3+}, Yb^{3+} upconverting nanoparticles, *Nanoscale*, 2010, **2**, 1417–1419.
36 D. O. Faulkner, S. Petrov, D. D. Perovic, N. P. Kherani and G. A. Ozin, Absolute quantum yields in NaYF4:Er,Yb upconverters – synthesis temperature and power dependence, *J. Mater. Chem.*, 2012, **22**, 24330.